

Gravitational Echoes from Braneworlds

Chun-Chun Zhu^{a b}, Jing Chen^{a b c}, Wen-Di Guo^{a b}, and Yu-Xiao Liu^{a b *}

^aLanzhou Center for Theoretical Physics,

Key Laboratory for Quantum Theory and Applications of the Ministry of Education,

Key Laboratory of Theoretical Physics of Gansu Province,

School of Physical Science and Technology,

Lanzhou University, Lanzhou 730000, China

^bInstitute of Theoretical Physics and Research Center of Gravitation,

School of Physical Science and Technology,

Lanzhou University, Lanzhou 730000, China

^cScience and Technology on Vacuum Technology and Physics Laboratory,

Lanzhou Institute of Physics,

Lanzhou, 73000, China

Abstract

Gravitational echoes can be used to probe the structure of spacetime. In this paper, we investigate the gravitational echoes in different braneworld models in five-dimensional spacetime. We derive the gravitational perturbation equations of these models, and obtain the time-dependent evolution equations of the extra-dimensional and radial components. Using a Gaussian wave packet as initial data, we study the time evolution of the gravitational perturbation. By monitoring the evolution of the Gaussian wave packet, the gravitational echoes are observed whether the wave packet is generated from inside or outside the braneworld. Furthermore, we can restrict the parameters of the braneworld by calculating the strength of the first gravitational echo and using the current gravitational wave data.

PACS numbers:

* liuyx@lzu.edu.cn, corresponding author

I. INTRODUCTION

In 2015, Laser Interferometer Gravitational-Wave Observatory (LIGO) detected the first gravitational wave signal GW150914, originating from the merger of a binary black hole system [1]. This groundbreaking event paved the way to do new researches on gravitational wave astronomy [2–9]. The GW150914 signal was generated from the merger of two black holes with about 36 solar masses and 29 solar masses into a final black hole with about 62 solar masses [1]. Binary black hole merger can be divided into three stages: inspiral, merger, and ringdown. Of particular interest to us is the final ringdown stage, as it contains crucial information about the structure of the final black hole.

The signal from the ringdown stage is generally composed of quasinormal modes of the black hole [10–12]. Regge and Wheeler first introduced the concept [13] of quasinormal modes when they studied gravitational perturbations of the Schwarzschild black hole. A set of discrete quasinormal frequencies was found in their pioneering work [11–13]. The presence of discrete frequencies is due to the radiation boundary conditions imposed at the black hole’s event horizon and at infinity. In the classical theory, quasinormal modes could reflect the spacetime structure near the black hole horizon. However, is there a more complex quantum structure near the black hole horizon? Or could it possibly be other exotic compact objects instead of black holes? How can these questions be addressed through gravitational waves? It has been recently argued [14] that although the early stages of the ringdown signal from compact objects are similar to those from black holes, modifications to the quantum structure near the horizon or alterations to the horizon itself may manifest in secondary pulses during the later stages of the ringdown. The reason is that the effective potential of gravitational perturbations in typical black hole models only has a single barrier, leading to a monotonic decay in the amplitude of signals during the ringdown [11, 13, 15–18]. On the other hand, quantum structures near the black hole horizon [19–22], such as firewalls [21, 22], may introduce new barriers to the effective potentials for gravitational perturbations near the horizon. Additionally, other horizonless compact objects, such as wormholes [14, 23], would exhibit multiple barriers in their effective potentials for gravitational perturbations. In such cases, although quasinormal modes still manifest as discrete quasinormal frequencies, some of these modes decay at a relatively slower rate, which could lead to the observation of multiple peaks in the signal. This occurs as the signal can be

reflected multiple times by these barriers, generating a scattering resonance effect where the segment of signal with the resonance frequency will be quasi-localized between the barriers. This phenomenon results in multiple similar signal peaks, termed gravitational echoes [24–31]. Therefore, detecting gravitational echoes can provide strong evidence for the existence of these previously undiscovered structures.

The extra-dimensional theories fundamentally alter our perspective on the concept of spacetime structure. These theories aim to either unify gravity and electromagnetism [32, 33] or solve the gauge hierarchy problem (the fine-tuning problem) in the standard model of particle physics [34–37]. In the models addressing the hierarchy problem, Randall-Sundrum 1 (RS-1) model [35] stands out as more refined candidates and has successfully addressed the hierarchy problem. Based on it, RS-2 and thick brane models with an infinite extra dimension can restore the four-dimensional Newtonian potential [36–57]. In most extra-dimensional theories, we can observe that the effective potential felt by gravitational perturbations often features multiple barriers [37–57]. Consequently, the possibility of gravitational echoes in these models becomes significantly high. Our research aims to study the gravitational echoes in various thick brane models. We use Gaussian wave packets as initial waveforms and employ numerical simulation to monitor their evolution and observe whether gravitational echoes occur. Furthermore, we simulate the waveform of Gaussian wave packets propagating along the brane, and calculate the time interval between the secondary pulse and the primary wave. It is worth noting that LIGO claims to have no evidence for the existence of quasinormal modes or gravitational echoes [1, 58–63]. It indicates that either the secondary pulse or echoes must be sufficiently weak or the time interval between secondary pulse and the primary wave is sufficiently large, exceeding the detection ability of current detectors. Therefore, these observational outcomes impose certain restrictions on the parameter settings of extra-dimensional models.

The remaining part of this paper is organized as follows. In Sec. II, we study the gravitational echoes from a thick brane generated by a canonical scalar field in five-dimensional general relativity framework. In Sec. III A and Sec. III B, we study the gravitational echoes in $f(R)$ gravity and the non-minimally derivative coupled scalar-tensor gravity in five-dimensional spacetime, respectively. Finally, we give the discussions and conclusions in Sec. IV.

II. FIVE-DIMENSIONAL THICK BRANE MODEL

In this section, we investigate the gravitational echoes from a flat thick brane that is generated by a canonical scalar field and has a flat 3-brane under the five-dimensional general relativity framework. First, we consider the five-dimensional gravity action with a real scalar field [37]:

$$S = \int d^5x \sqrt{-g} \left[\frac{M_5^3}{4} R - \frac{1}{2} \partial_M \phi \partial^M \phi - V(\phi) \right]. \quad (1)$$

where the capital Latin letters $M, N, \dots = 0, 1, 2, 3, 5$ label the five-dimensional spacetime indices. In this paper we set $M_5^3/4=1$. By varying the action (1) with respect to the metric and the scalar field respectively, we can obtain the equations of motion:

$$G_{MN} = T_{MN}^{(\phi)}, \quad (2)$$

$$\square \phi = \frac{dV(\phi)}{d\phi}, \quad (3)$$

where $T_{MN}^{(\phi)} = \partial_M \phi \partial_N \phi - g_{MN} (\frac{1}{2} \partial_M \phi \partial^M \phi + V(\phi))$ is the energy-momentum tensor of the scalar field and $\square = g^{MN} \nabla_M \nabla_N$. The five-dimensional metric describing a static flat brane is [35, 36, 64–67]

$$ds^2 = e^{2A(y)} \eta_{\mu\nu} dx^\mu dx^\nu + dy^2, \quad (4)$$

where y is the extra-dimensional coordinate and $e^{2A(y)}$ is the warp factor. Here, Greek letters $\mu, \nu, \dots = 0, 1, 2, 3$ label the four-dimensional spacetime indices. With metric (4), we can write the specific form of the field equations:

$$6A'' + 12A'^2 + 2V(\phi) + \phi'^2 = 0, \quad (5)$$

$$6A'^2 + V(\phi) - \frac{1}{2}\phi'^2 = 0, \quad (6)$$

$$\phi'' + 4A'\phi' - \frac{dV(\phi)}{d\phi} = 0, \quad (7)$$

where prime denotes the derivative with respect to the extra-dimensional coordinate y . We can also derive Eq. (7) through $\nabla^M T_{MN}^{(\phi)} = 0$. So only two of the above three equations are independent. Considering the following boundary conditions: $A(0) = 0$, $A'(0) = 0$,

$\phi(y) = -\phi(-y)$, and $\phi(\pm\infty) \rightarrow \text{const}$, we can get the following solutions:

$$\phi(y) = v \tanh(ky), \quad (8)$$

$$A(y) = -\frac{1}{18}v^2 \tanh^2(ky) - \frac{2}{9}v^2 \ln(\cosh(ky)), \quad (9)$$

$$V(\phi) = \frac{k^2}{54v^2} [4\phi^6 - 3(8v^2 + 9)\phi^4 + 18v^2(2v^2 + 3)\phi^2 - 27v^4], \quad (10)$$

where k and v are real parameters. The distributions of the warp factor, the scalar field, and the scalar potential are shown in Fig. 1. The configuration of the scalar field (8) is a

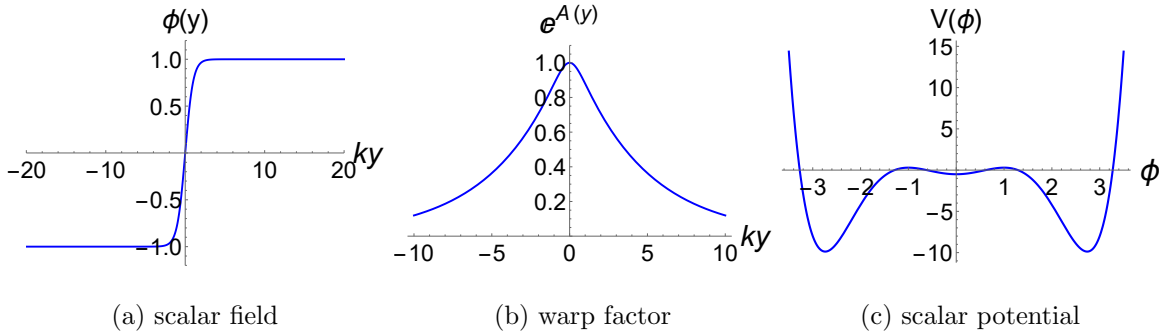


Figure 1: Plots of the single kink scalar field, the warp factor, and the scalar potential with $v = 1$.

single kink as shown in Fig. 1(a). However, it should be pointed out that a double kink scalar field is also the solution of the field equations under the above boundary conditions. The solution of a double kink scalar field can be taken as

$$\phi(y) = v (\tanh(ky + b) + \tanh(ky - b)), \quad (11)$$

where b is the dimensionless distance between the two kinks of the scalar field. Now, since there is no analytical solution for the warp factor and the scalar potential, they can only be depicted numerically. The range of $\phi(y)$ is $(-2v, 2v)$ when y belongs to $(-\infty, \infty)$.

The distributions of the warp factor, the scalar field, and the scalar potential are shown in Fig. 2. It can be seen that as the distance b between the two kinks of the scalar field increases, the warp factor appears to plateau and its width also increases. The value of the scalar potential at $\phi = 0$ increases with b . As the distance b approaches infinity, the value of $V(0)$ approaches zero, and the values on both sides will decrease accordingly.

Next we consider gravitational perturbations on the brane with the RS gauge $h_{(M0)} = 0$. Since the scalar, vector, and tensor modes are decoupled from each other, we just focus on the tensor perturbation:

$$ds^2 = e^{2A(y)}(\eta_{\mu\nu} + h_{\mu\nu})dx^\mu dx^\nu + dy^2. \quad (12)$$

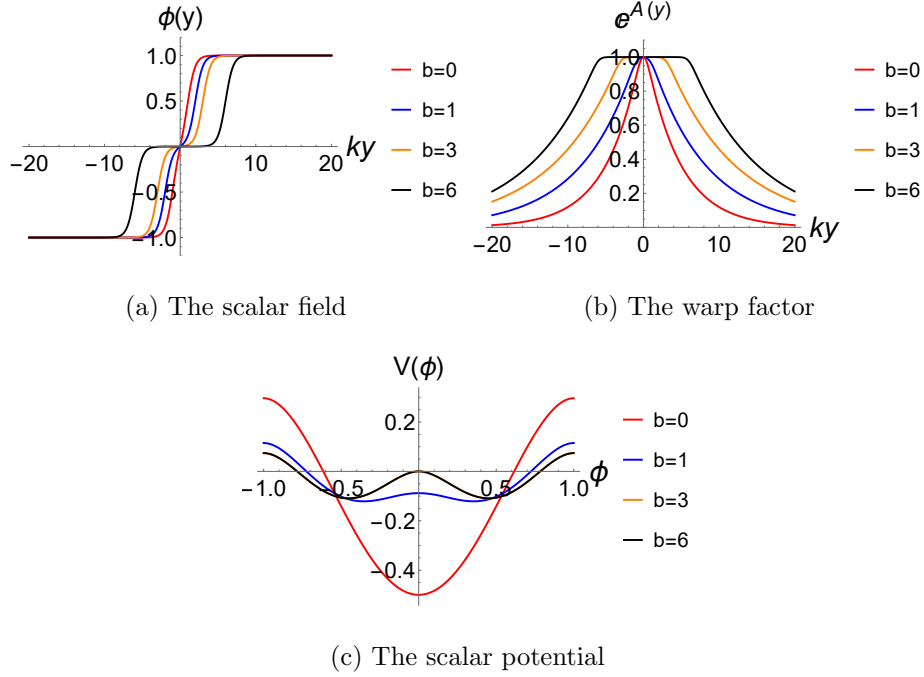


Figure 2: Plots of the double kink scalar field, the warp factor, and the scalar potential with $v = 0.5$ and $k = 1$.

We consider the transverse and traceless (TT) gauge $\eta^{\mu\alpha}\partial_\alpha h_{\mu\nu} = \eta^{\mu\alpha}h_{\mu\nu} = 0$ and make the transformation $dy = e^A dz$. Then, by redefining $h_{\mu\nu} = e^{-3A(z)/2}\tilde{h}_{\mu\nu}$, the perturbation equation can be obtained:

$$\square_{(4)}\tilde{h}_{\mu\nu} - \partial_z^2\tilde{h}_{\mu\nu} + V_{\text{eff}}(z)\tilde{h}_{\mu\nu} = 0, \quad (13)$$

where $\square_{(4)} = \eta^{\mu\nu}\partial_\mu\partial_\nu$ and the effective potential is

$$V_{\text{eff}}(z) = \frac{3}{2}\partial_z^2 A + \frac{9}{4}(\partial_z A)^2. \quad (14)$$

Then we do the following decomposition $\tilde{h}_{\mu\nu}(t, x^i, z) = \varepsilon_{\mu\nu}(x^i)H(t, z)$. The evolution equation of the extra-dimensional component is

$$\partial_t^2 H(t, z) - \partial_z^2 H(t, z) + V_{\text{eff}}(z)H(t, z) = -p^2 H(t, z), \quad (15)$$

where p^2 satisfies $\partial_i^2 \varepsilon_{\mu\nu} = -p^2 \varepsilon_{\mu\nu}$. Then, by considering the further decomposition $H(t, z) = \psi(z)e^{i\omega t}$, we can rewrite Eq. (15) as

$$-\partial_z^2 \psi(z) + V_{\text{eff}}(z)\psi(z) = m^2 \psi(z), \quad (16)$$

where $m^2 = \omega^2 - p^2$. When $m = 0$, the zero mass mode can be obtained:

$$\psi_0(z) = N_0 e^{3A/2}. \quad (17)$$

For the single kink solution, when $y \rightarrow \pm\infty$, $A(y) \rightarrow \mp \frac{2kv^2}{9}y$. It is easy to show that $\int_{-\infty}^{+\infty} \psi_0^2(z)dz = N_0^2 \int_{-\infty}^{+\infty} e^{2A(y)}dy < +\infty$. Thus, the zero mode is localized near the brane. For the double kink solution, the distribution of the zero mode is shown in Fig. 3. As b

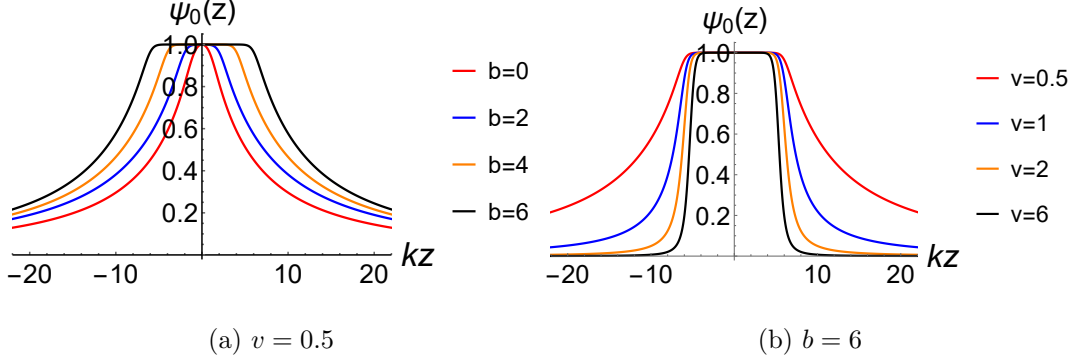


Figure 3: Plots of the zero mode (17) with different values of b and v for the double kink scenario.

increases, the trend on both sides of the zero mode remains the same, and the width of the platform near $y = 0$ increases with b . The greater the vacuum expectation value v of the scalar field, the steeper the peak of the zero mode. The effective potential V_{eff} with different values of b and v is shown in Fig 4. The distance between the two barriers increases with b and the height of barriers increases with v .

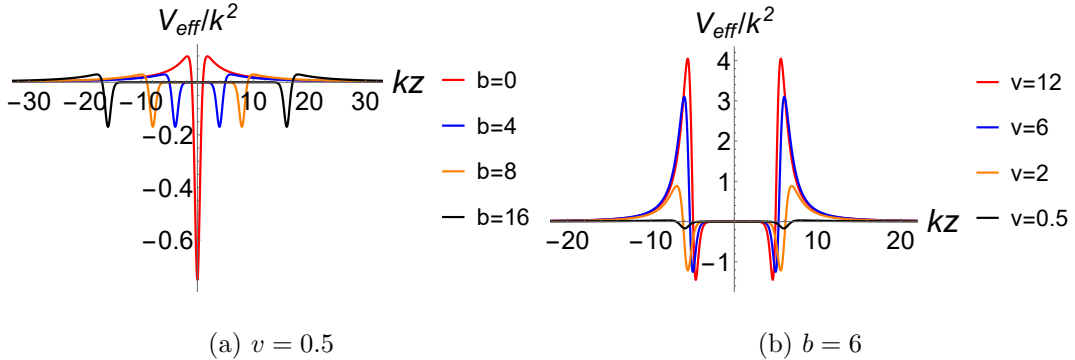


Figure 4: Plots of the effective potential (14) with different values of v and b for the double kink scenario.

Next, we investigate the evolution of a Gaussian packet. The evolution equation is given by Eq. (15), and the boundary conditions can be selected to be the radiative boundary conditions [68]. We initialize the system with a right-moving Gaussian wave packet $H(0, z) = e^{-\frac{(z-z_0)^2}{\sigma}}$ traveling at the speed of light as the initial condition. The evolution behaviors of different Gaussian wave packets at a fixed point of extra dimension are shown in Figs. 5 and 6.

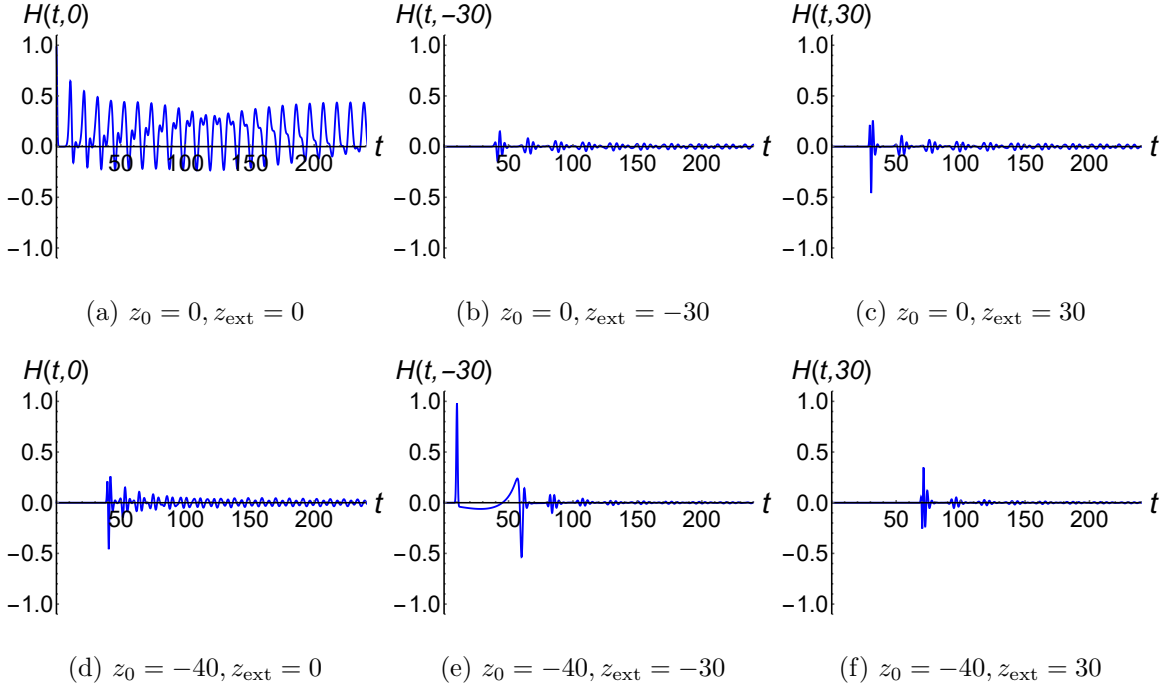


Figure 5: Plots of the evolution $H(t, z)$ of different Gaussian wave packets located at different positions z_{ext} . The parameters of the double kink scalar and Gaussian wave packet are $b = 6$, $v = 6$ and $\sigma = 0.5$.

Figure 5 illustrates the evolutionary behavior of Gaussian wave packets positioned at various locations: $z_0 = 0$ (inside the potential well) and $z_0 = -40$ (outside the potential well). In Figs. 5(a) and 5(d), it can be seen that the echoes are not distinct for Gaussian wave packets whether they are located inside or outside the potential well. The reason is that, for the signal within the potential well, the wave packet encounters reflections from both barriers. Additionally, the difference between the widths of the wave packet and the potential well is small. Consequently, the time intervals between the reflected pulses are small. The echo phenomenon in other subgraphs is relatively obvious. Figure 6 shows the effect of the vacuum expectation value v and the distance b between the two kinks of the scalar field on the echoes. The larger the distance between the two kinks, the greater the time interval among the echoes. The larger vacuum expectation value v , the larger the amplitude of the first echo, and the smaller the amplitude of the subsequent echoes. However, it results in smaller amplitude for the subsequent echoes, though with a slower rate of attenuation. The echoes occur because a wave with the resonant frequency is reflected back and forth within the cavity, with a portion being transmitted during each reflection. The amplitude of the primary wave is the largest, while the amplitudes of the subsequent

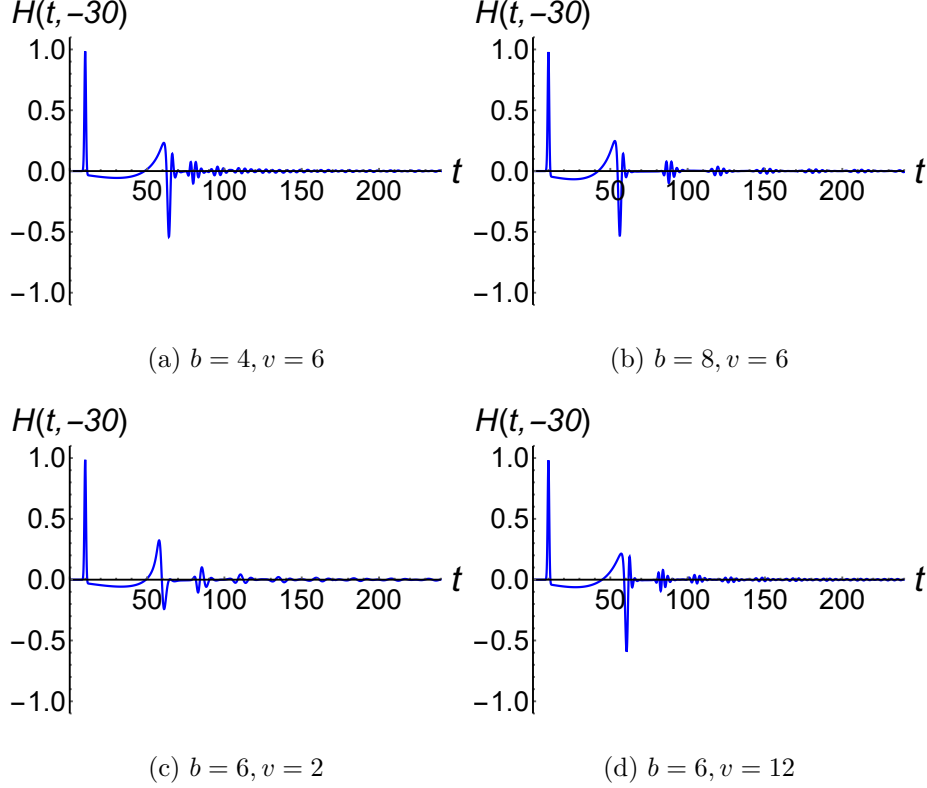


Figure 6: Plots of the evolution $H(t, z)$ of the Gaussian wave packets for different values of the parameters of the double kink scalar field. The parameters of the Gaussian wave packet are set to $z_0 = -40$ and $\sigma = 0.5$.

echo pulses gradually decrease. Due to the high reflectivity of the barrier, the amplitude decay in the quasi-potential well is slow, as evidenced in the left panel of Fig. 5. We can perform spectral analysis of the waveform to demonstrate this point,

$$F[\tilde{H}(f, z_{\text{ext}})] = \left| A \sum_p H(t_p, z_{\text{ext}}) e^{-i2\pi f t_p} \right|, \quad (18)$$

where $A = 1/\max(F[\tilde{H}(f, z_{\text{ext}})])$ is a normalized constant, and z_{ext} is a fixed point. We use the transfer matrix to calculate the transmittance spectra.

Figure 7 shows the frequency spectra of the waveforms illustrated in Figs. 5(d) and 5(e) and the transmittance of the gravitational perturbations under the effective potential (14). The frequency spectrum of the waveform at an internal point $z_0 = 0$ of the potential well is shown in Fig. 7(a). Due to the formation of a resonant cavity by the two barriers of the potential, the internal waves undergo multiple reflections from these barriers. Therefore, the wave in the resonant cavity has low transmittance (and consequently high reflectivity). The

frequency spectrum of the waveform at an external point $z_0 = -30$ is shown in Fig. 7(b). Its frequencies have no obvious pattern. To analysis this complex spectrum, we calculate and present frequency spectra for different time intervals in Figs. 7(c)-7(f). The frequency spectrum for the early time interval $t = 0 \sim 100$ is shown in Fig. 7(c). This waveform contains the first three pulses, that can be seen from Fig. 5(e). The frequency distribution of this waveform is roughly similar to Fig. 7(b). Later signals are mainly the echo pulses. The later the echo appears, the lower its transmittance, which can be seen in Figs. 7(d)-7(f). The reason is that, echoes are the part of the wave that is transmitted from the potential well. The more times the wave is reflected back and forth by the two barriers, the greater the reflection coefficient of the echoes. The frequencies of the high reflectivity echoe in the late-time stages can be utilized as characteristic frequencies to comprehend the spacetime structure of extra dimensions.

The expression for the effective stress-momentum tensor of gravitational waves is given by [69, 70]

$$T_{MN} = \frac{1}{32\pi} \langle \partial_M h^{\mu\nu} \partial_N h_{\mu\nu} \rangle, \quad (19)$$

where the angular brackets $\langle \dots \rangle$ denote a spatial average over several wavelengths. By using the stress-energy tensor T_{MN} and the time-like killing vector $k^N = (e^{-A}, 0, 0, 0, 0)$, the conserved current is given by

$$J_M = T_{MN} k^N. \quad (20)$$

Then we can define the energy of the gravitational perturbation [71]:

$$E = \int J^0 \sqrt{-g} d^3 x dz. \quad (21)$$

Assuming the gravitational perturbation is a plane wave on the brane, we solely focus on the evolution of the extra dimensional component. Consequently, we separate the energy into two parts as follows,

$$E = \varepsilon_b \times \varepsilon_e, \quad (22)$$

where

$$\varepsilon_b = \frac{1}{32\pi} \int \epsilon_{\mu\nu} \epsilon^{\mu\nu} d^3 x, \quad (23)$$

$$\varepsilon_e = \int_{-z_b}^{z_b} (\partial_t H(t, z))^2 dz. \quad (24)$$

In the following part, we only focus on the extra-dimensional part ϵ_e .

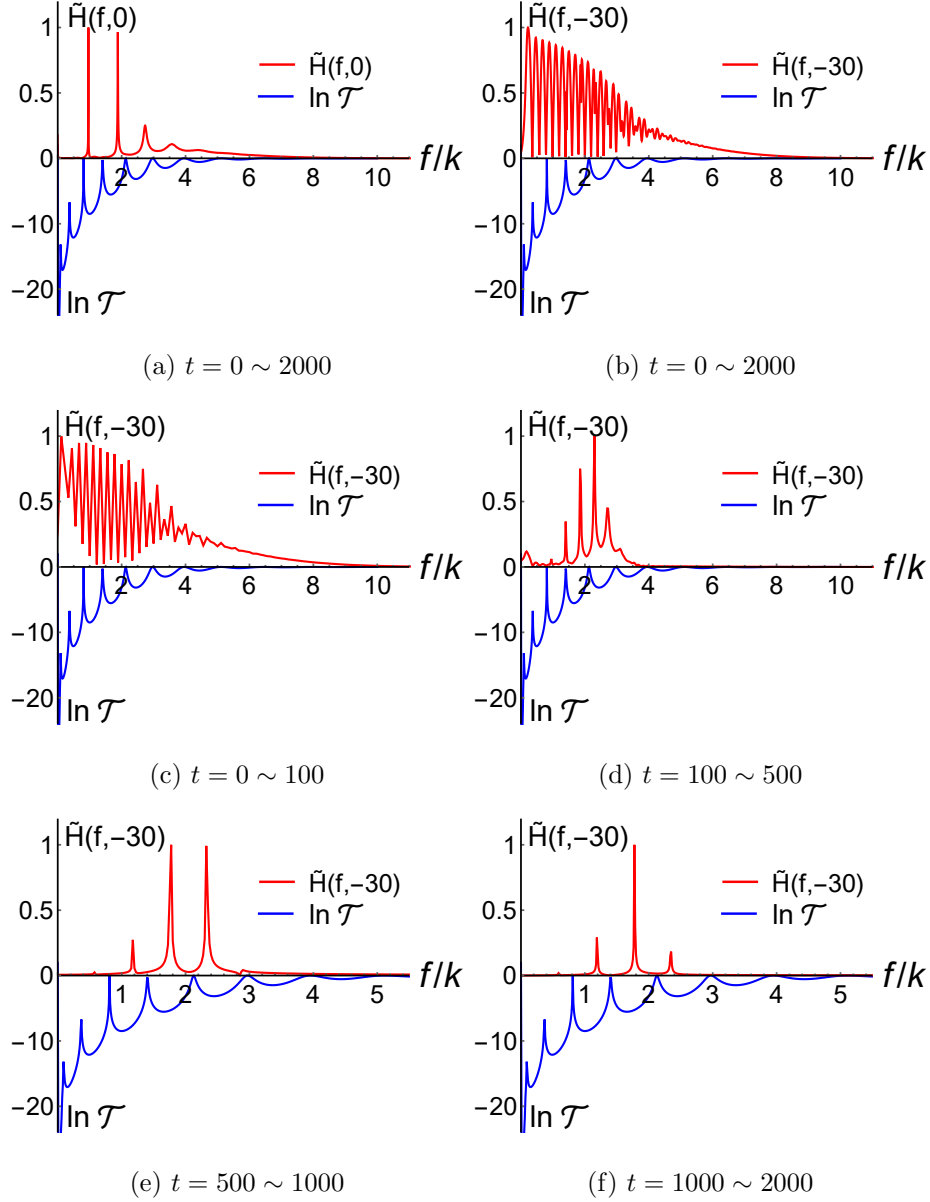


Figure 7: Plots of the Fourier transform spectra of the waveforms in Figs. 5(d) and 5(e) within different time intervals, and the transmittance \mathcal{T} under the effective potential (14) with parameters $b = 6$ and $v = 6$.

Figure 8 illustrates the energy evolution of an initial wave packet both inside and outside the potential well. Interval 1 represents the whole interval of evolution and interval 2 represents the region of the brane or the quasi well. Figure 8(a) shows the energy evolution of the wave packet initially located in the interval 2. The initial energy of the wave packet is localized inside the interval 2. However, as a part of the wave propagates out of the interval 2, the energy of the signal on the brane will decrease. Figure 8(b) illustrates the energy

evolution of the wave packet initially located outside the interval 2 but in the interval 1. After some time, a part of the wave passes through the barrier and enters the potential well, thus the energy of the wave packet on the brane will increase. Then as the wave propagates out the interval 2, the energy inside the interval 2 will decrease. It can be seen that, both the energy in the interval 1 and interval 2 decrease in a step-like manner. This is because echo pulses are generated one after another, and whenever an echo pulse propagates out of the interval 1 or 2, the energy of the wave rapidly decreases. In later stages, the energies of the two intervals will be almost the same, as only the waves quasi-localized on the brane slowly leak out.

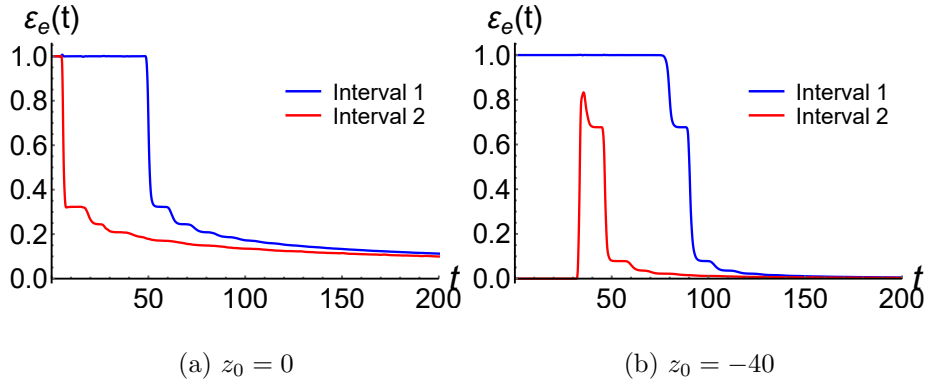


Figure 8: Plots of the evolution of energy with different Gaussian wave packets. Interval 1 represents $(-z_b, z_b) = (-50, 50)$ (the whole interval of evolution) and interval 2 represents $(-z_b, z_b) = (-6, 6)$ (inside the brane). The parameters of the double kink scalar and the Gaussian wave packet are set to $b = 8$, $v = 6$, and $\sigma = 0.5$.

To explain the problem of the number of peaks per pulse in subsequent pulses, we use the finite high square barrier as a toy model. We also choose the Gaussian wave packet $H(0, z) = e^{-\frac{(z-z_0)^2}{\sigma}}$ as the initial data with the parameters $z_0 = -40$ and $\sigma = 1$. The square barrier function is

$$V_{\text{eff}}(z) = \begin{cases} h, & -\beta \leq z \leq \beta, \\ 0, & \text{otherwise,} \end{cases} \quad (25)$$

where 2β and h are the width and the height of the barrier, respectively. The shape of the square barrier is shown in the left panel of Fig. 9.

Figure 10 illustrates the impact of the width and height of the square barrier on the evolution of wave packets. It can be seen that the number of peaks of the subsequent pulse is actually infinite. However, the greater the barrier width, the more pronounced the peaks

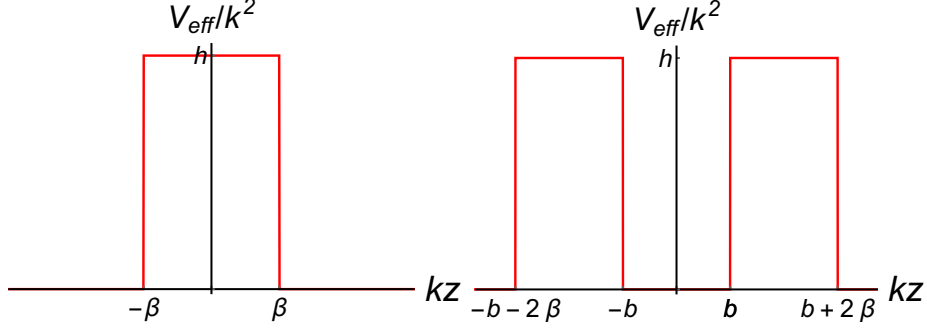


Figure 9: Plots of the single and the double barrier potentials.

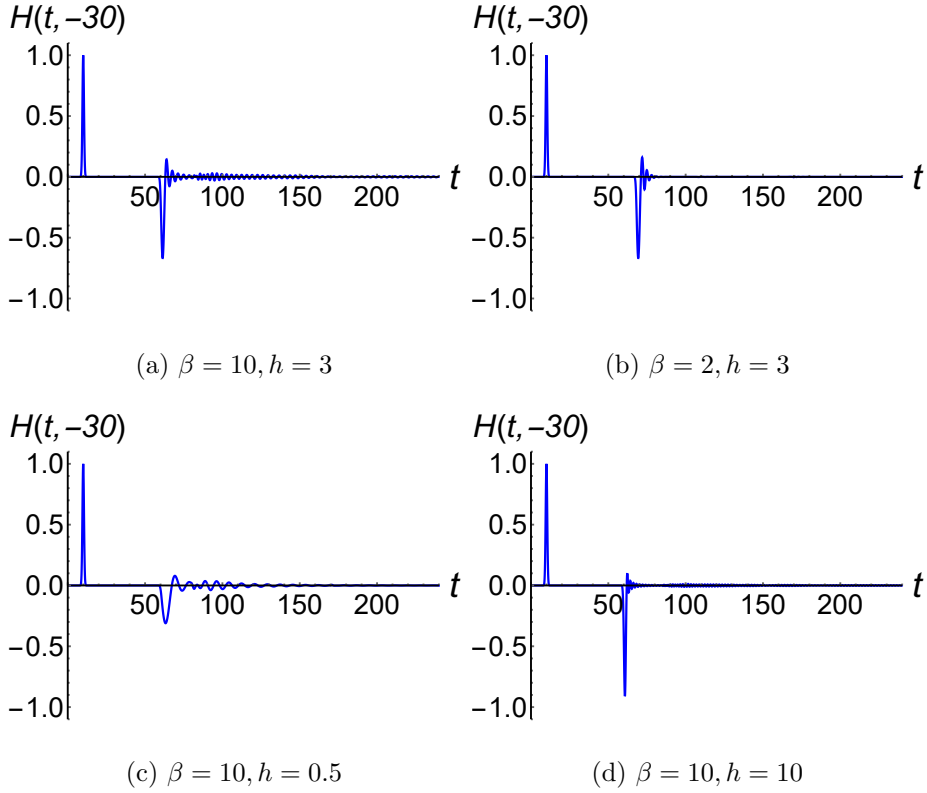


Figure 10: Plots of the evolution $H(t, z)$ of a Gaussian wave packet under the single barrier. The parameters of the Gaussian wave packet are set to $\sigma = 0.5$ and $z_0 = -40$.

of the subsequent pulses. The higher the height of the barrier, the larger the height of the first reflected peak, and conversely the weaker the subsequent peaks. We also simulate the wave packet evolution under the double barriers. The barrier function is

$$V_{\text{eff}} = \begin{cases} h, & b < |z| < b + 2\beta, \\ 0, & \text{otherwise,} \end{cases} \quad (26)$$

which can be seen in the right panel of Fig. 9.

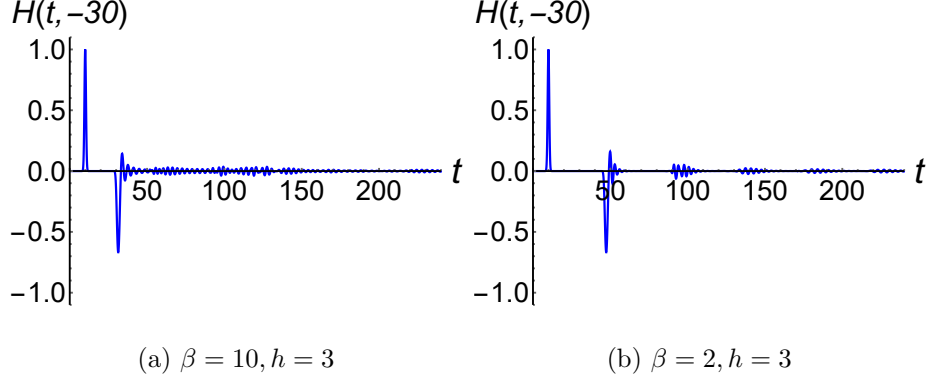


Figure 11: Plots of the evolution $H(t, z)$ of a Gaussian wave packet under the double barriers. The parameters of the Gaussian wave packet are set to $\sigma = 0.5$ and $z_0 = -40$.

As can be seen in Fig. 11, the signals have comparatively obvious echoes in the case of double barriers. The smaller the width of the barriers, the shorter the pulse signal, and the more pronounced the echoes.

In the previous part, we only focus on the extra-dimensional component of the gravitational wave. However, the matter of our universe is localized on the brane, and we can not observe the signal out of the brane. Consequently, we explore the phenomenon of the gravitational echoes when the gravitational wave propagates on the brane. The coordinate on the brane is chosen to be three-dimensional spherically symmetric coordinates (r, θ, φ) . By separating the angle part from the other parts $\tilde{h}_{\mu\nu} = \sum_{lm} \frac{1}{r} R_{lm}(t, r, z) (Y_{lm})_{\mu\nu}(\theta, \varphi)$, we can get the evolution equation of the extra and radial components from Eq. (13),

$$\partial_t^2 R(t, r, z) - \partial_r^2 R(t, r, z) - \partial_z^2 R(t, r, z) + V_{\text{eff}}(z) R(t, r, z) = -\frac{l(l+1)}{r^2} R(t, r, z). \quad (27)$$

In the following, we consider the spherical wave $l = 0$. Similarly, we also consider a Gaussian wave packet $R(0, r, z) = e^{-\frac{z^2+r^2}{\sigma}}$ as the initial waveform, and take the radiative boundary conditions. In the numerical program of two-dimensional evolution, the radiation boundary condition ($\partial_t R = \partial_\rho R$ for $\rho \rightarrow \infty$, where $\rho = \sqrt{r^2 + z^2}$ is the four-dimensional spherical coordinate) cannot completely suppress the waves reflected from the boundary due to numerical errors, so some modifications listed as follows are adopted [72]:

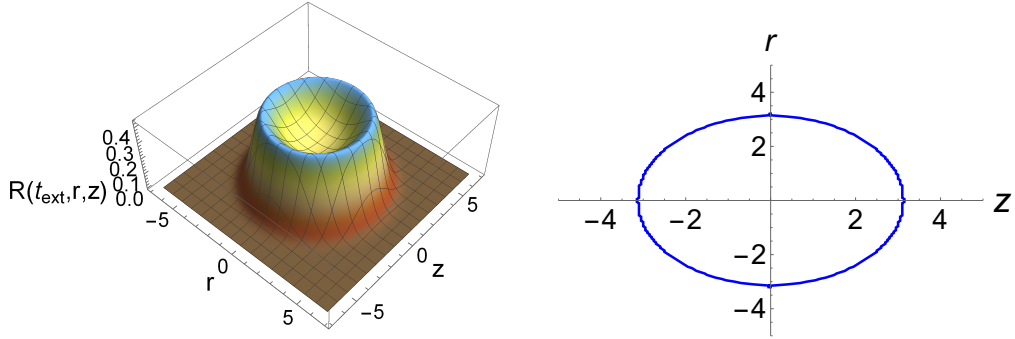
$$\begin{aligned} \frac{z}{\sqrt{r^2 + z^2}} \partial_t R \pm \partial_z R \pm \frac{z}{(r^2 + z^2)} R &\simeq \frac{z h'(t)}{(r^2 + z^2)^{\frac{N+1}{2}}}, \quad z \rightarrow \pm\infty, \\ \frac{r}{\sqrt{r^2 + z^2}} \partial_t R \pm \partial_r R \pm \frac{r}{(r^2 + z^2)} R &\simeq \frac{r h'(t)}{(r^2 + z^2)^{\frac{N+1}{2}}}, \quad r \rightarrow \pm\infty, \end{aligned}$$

where $h(t)$ is a time function that resolves transient errors and N is an optional parameter. In general, the value of $h(t)$ is calculated at the non-boundary position and subsequently applied at the boundaries. When $N = 3$, the error is best eliminated.

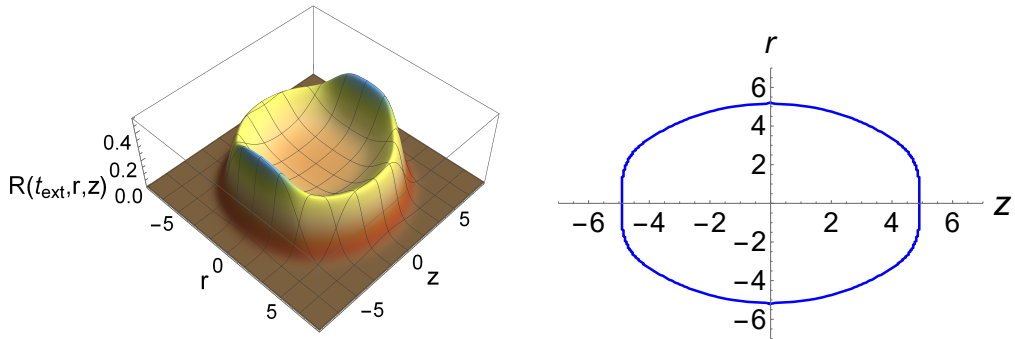
The left panels of Fig. 12 show the two-dimensional distributions of the gravitational waveforms at different times. Additionally, we also use the peak point of the pulse signal to depict the position of the wave front at different times, as shown in the right panels of Fig. 12. The waveform at early time $t = 3$ only has a single peak in Fig. 12(a). Subsequently, at $t = 5$, the waveform at $z = \pm 5$ exhibits a slight deformation from a spherical wave which can be seen in Fig. 12(b). Furthermore, at $t = 10$, as Fig. 12(c) shows, in addition to the outermost primary wave ($r \sim 10$) on the brane, there is also a wave peak (echo) on the brane due to the reflection of the wave packet on the barrier. Lastly, at $t = 20$, the echoes also appear outside the brane, and more complex echo waves appear on the brane due to the barrier reflection, which can be seen in Fig. 12(d). We can clearly observe the multiple pulses outside the barrier. There are also echoes produced by the reflection of the Gaussian wave packet in the potential well. Due to the high reflectivity under the effective potential (14), the signal inside the potential well is much stronger than the signal outside the potential well.

Figure 13 depicts a schematic diagram of the propagation path of the gravitational waves along the brane. It also illustrates the propagation of the first three pulses from the wave source to the observation point. It should be noted that, the generation of gravitational echoes in the extra-dimensional model occurs during the propagation path due to reflection by the potential barrier and is independent of the wave source. The gravitational echoes for compact stars are generated near the stars, which depends on the structure of the stars. The orange line represents the wave traveling in a straight line, the red lines represent the wave reflected once by the barrier, which constitutes the first echo signal, and the blue lines represent the wave reflected twice by the barrier, which constitutes the second echo signal. From this we can calculate the time interval between the n -th echo signal and the primary wave signal. If the distance between the barriers is $2d$ and the distance between the source and the observer is l , then the time interval between the n -th gravitational echo and the primary wave is

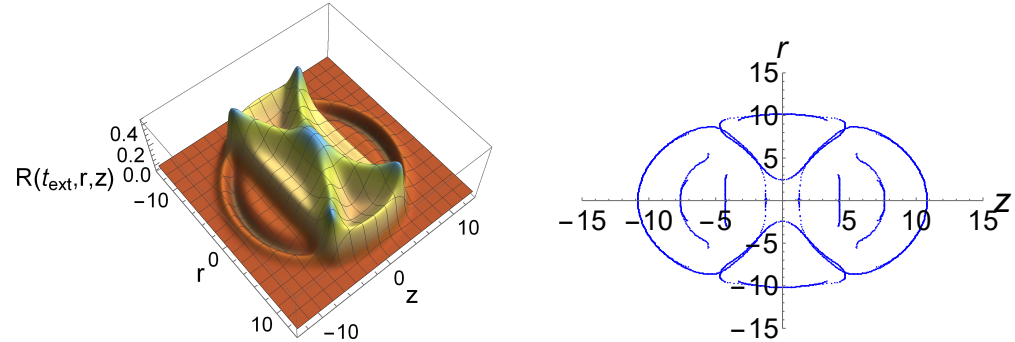
$$t_n = \frac{2n\sqrt{\left(\frac{l}{2n}\right)^2 + d^2} - l}{c}. \quad (28)$$



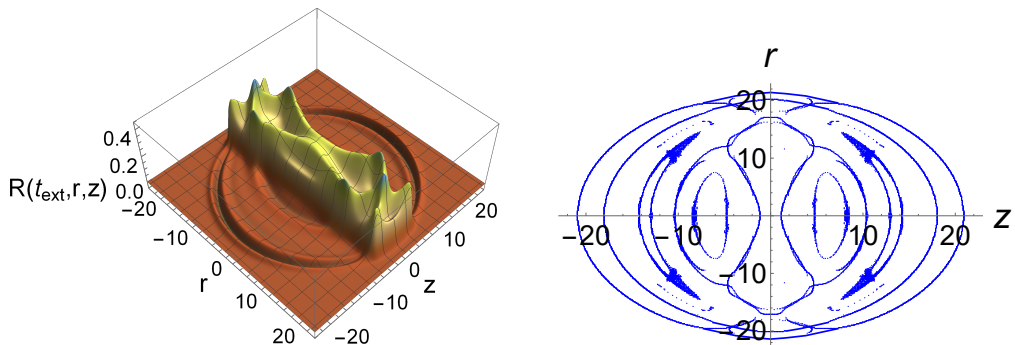
(a) $t = 3$



(b) $t = 5$



(c) $t = 10$



(d) $t = 20$

Figure 12: Plots of the evolution $R(t, r, z)$ of a two-dimensional Gaussian wave packet and the wave front of gravitational waves at different time. The parameters are set to $b = 6$, $v = 6$, and $\sigma = 1$.

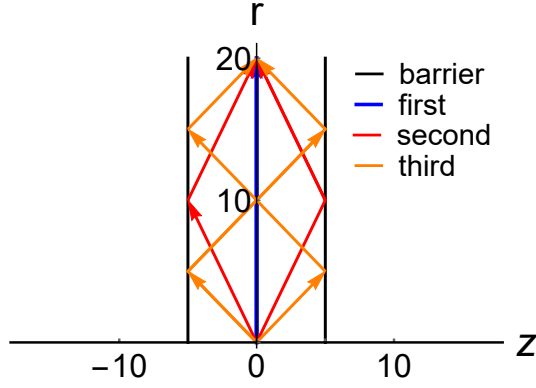


Figure 13: Plot of the propagation path of the gravitational waves. The blue, red, and orange lines represent the propagation path of the first three pulses, respectively.

In Fig. 12, we can also observe the wavefront at different positions simultaneously. When $t = 20$, the primary wave propagating along r is roughly at $r = 20$, and the position of the first echo is roughly at $r = 17$, which is fundamentally consistent with the formula (28). Note that the position of the reflecting surface is approximately at $z = 4.6$. When $l \gg d$, Eq. (28) becomes $t_n(l \gg d) \approx 4n^2d^2/(lc)$. Since no echo signal was detected in the first gravitational wave event, GW150914, there are two possibilities for this model. One is that the distance d between the two barriers is too large, so the arrival time interval between the secondary pulse and the primary wave is too large. The binary black hole signal from GW150914, is approximately 410Mpc away and the detectors operated for about 10 seconds [1]. From Eq. (28), the distance between the barriers $2d$ should be more than 20 light year. The second possibility is that the reflectivity is too low, and the signal strength of the secondary pulse is not enough to be detected. For LIGO, the minimum signal sensitivity of its detectors is approximately 1/10 of the signal amplitude of GW150914 [1]. Therefore, for the frequency range of the GW150914 signal (35-250Hz) [1], the reflectivity should be less than 1/10. Roughly speaking, the reflectivity decreases with the frequency, which can be seen from Fig. 7. (The transmittance increases with the frequency.) Thus, when $f \leq 35\text{Hz}$, if the reflectivity is less than 1/10, then the amplitude of the gravitational echoes can be beyond the detection accuracy of the detector. With this criterion, we can obtain the constraints on the five-dimensional fundamental mass. The relationship between the five-dimensional fundamental mass M_5 and the four-dimensional Planck mass M_4 is presented as follows:

$$M_4^2 = \frac{M_5^3}{k} \int_{-\infty}^{+\infty} e^{2A(ky)} d(ky). \quad (29)$$

Through the transfer matrix method, we can calculate the dimensionless critical frequency f_0/k , such that, when $f > f_0$, the reflectivity is less than 1/10. The maximum value of f_0 should be 35Hz, thus we can get the corresponding k . Through Eq. (29), we can get the maximum value of the five-dimensional fundamental mass.

b	6	6	6	4	6	8
v	2	6	12	6	6	6
f_0/k	5.03	9.30	12.46	9.05	9.30	10.50
M_5/TeV	3.02×10^4	2.58×10^4	2.40×10^4	3.06×10^4	2.58×10^4	2.21×10^4

Table I: The maximum of the five-dimensional fundamental mass corresponding to the parameters b and v of the scalar field.

Table I illustrates that the maximum value of the five-dimensional fundamental mass M_5 decreases with the vacuum expectation value v and the distance between kinks b of the scalar field. The values of b and v can be determined by the frequency of the late-time gravitational echoes by matching to the characteristic frequencies of the extra-dimensional model, provided that gravitational echoes can be detected in the future.

III. ECHOES IN OTHER EXTRA-DIMENSIONAL THEORY

There are also multiple barriers in the effective potential of gravitational perturbation in other thick brane theories. In this section, we investigate gravitational echo phenomena in two different thick brane theories that exhibit the obvious multiple barriers.

A. Echoes in Five-Dimensional $f(R)$ Theory

In this subsection, we investigate the echoes of the thick brane in $f(R)$ gravity. First, the action of the $f(R)$ brane is given by [73–75]

$$S = \int d^5x \sqrt{-g} \left(\frac{M_5^3}{4} f(R) - \frac{1}{2} \partial^M \phi \partial_M \phi - \frac{1}{2} \partial^M \varphi \partial_M \varphi - V(\phi, \varphi) \right). \quad (30)$$

Varying the action (30) with respect to the metric g_{MN} and using the flat brane metric (4), we get the equations of motion:

$$f(R) + 2f_R(4A'^2 + A'') - 6f'_R A' - 2f''_R = 2(\phi'^2 + \varphi'^2 + 2V), \quad (31)$$

$$-8f_R(A'' + A'^2) + 8f'_R A' - f(R) = 2(\phi'^2 + \varphi'^2 - 2V), \quad (32)$$

$$\phi'' + 4A'\phi' - \frac{\partial V(\phi)}{\partial \phi} = 0, \quad (33)$$

$$\varphi'' + 4A'\varphi' - \frac{\partial V(\varphi)}{\partial \varphi} = 0. \quad (34)$$

We consider the degenerate Bloch-brane solution [76]:

$$\phi(y) = v \frac{\sqrt{c_0^2 - 4} \sinh(2dvy)}{\sqrt{c_0^2 - 4} \cosh(2dvy) - c_0}, \quad (35)$$

$$\varphi(y) = \frac{2v}{\sqrt{c_0^2 - 4} \cosh(2dvy) - c_0}, \quad (36)$$

$$e^{2A(y)} = \left(\frac{\sqrt{c_0^2 - 4} - c_0}{\sqrt{c_0^2 - 4} \cosh(2dvy) - c_0} \right)^{4v^2/9} \times \exp \left[-\frac{4v^2 (c_0^2 - 4 - c_0 \sqrt{c_0^2 - 4})}{9 (\sqrt{c_0^2 - 4} - c_0)^2} \right] \times \exp \left[\frac{4v^2 (c_0^2 - 4 - c_0 \sqrt{c_0^2 - 4} \cosh(2dvy))}{9 (\sqrt{c_0^2 - 4} \cosh(2dvy) - c_0)^2} \right]. \quad (37)$$

In our calculations, the parameters are set as $a = d = 1$, $v = 2$, and $c_0 = -2 - 7.0 \times 10^{-16}$ [75].

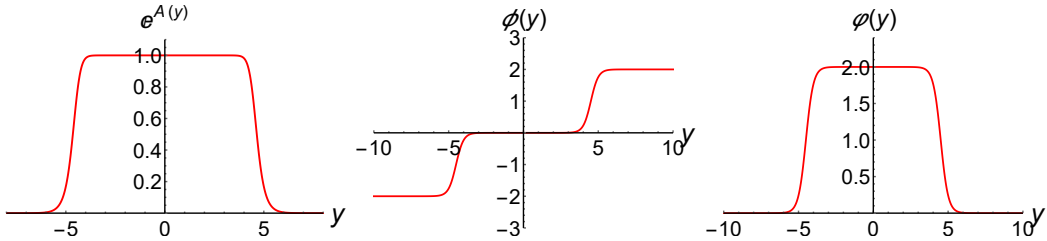


Figure 14: Plots of the warp factor and the two scalar fields.

Next we consider gravitational perturbations on the brane with RS gauge $h_{M0} = 0$. The metric describing the tensor perturbation is

$$ds^2 = e^{2A(y)} (\eta_{\mu\nu} + h_{\mu\nu}) dx^\mu dx^\nu + dy^2. \quad (38)$$

With the coordinate transformation $dz = e^{-A(y)} dy$, the perturbed Einstein equation reads

$$\left[\partial_z^2 + \left(3 \frac{\partial_z a}{a} + \frac{\partial_z f_R}{f_R} \right) \partial_z + \square^{(4)} \right] h_{\mu\nu} = 0. \quad (39)$$

where $a(z) = e^{A(z)}$. Then considering the following decomposition:

$$h_{\mu\nu}(t, x^i, z) = \epsilon_{\mu\nu}(x^i) a^{-3/2} f_R^{-1/2} H(t, z), \quad (40)$$

we obtain the evolution equation for the extra-dimensional component of the perturbation:

$$[\partial_t^2 - \partial_z^2 + V_{\text{eff}}(z)] H(t, z) = -p^2 H(t, z), \quad (41)$$

where

$$V_{\text{eff}}(z) = \frac{3}{4} \frac{(\partial_z a)^2}{a^2} + \frac{3}{2} \frac{\partial_z^2 a}{a^2} + \frac{3}{2} \frac{\partial_z a \partial_z f_R}{a f_R} - \frac{1}{4} \left(\frac{\partial_z f_R}{f_R} \right)^2 + \frac{1}{2} \frac{\partial_z^2 f_R}{f_R^2}. \quad (42)$$

We still take the same radiative boundary conditions as in Sec. II, and use a Gaussian wave

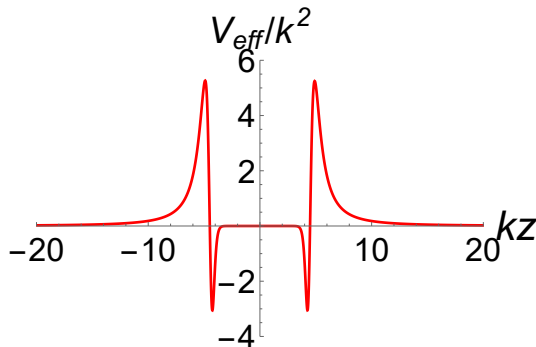
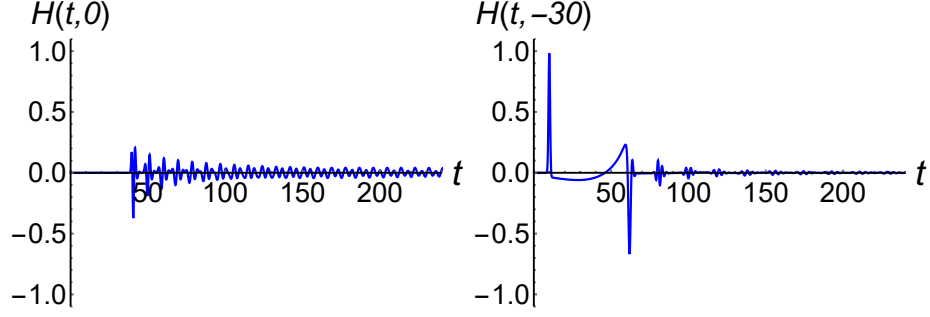


Figure 15: Plots of the effective potential (42) of the $f(R)$ brane.

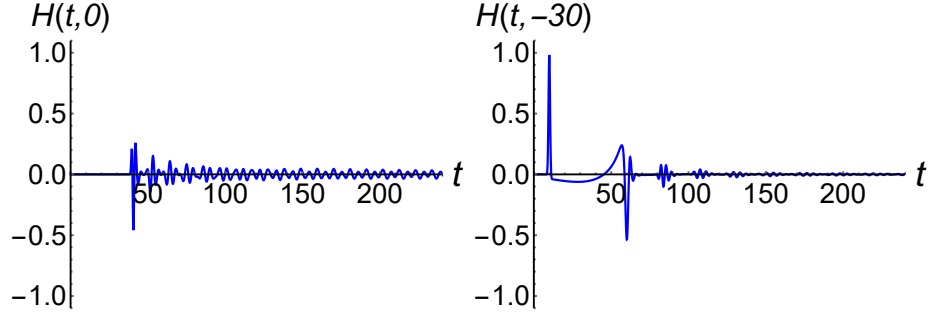
packet $H(0, z) = e^{-\frac{(z-z_0)^2}{\sigma}}$ for evolution. In Fig. 16, it can be seen that the evolution of the Gaussian wave packet is basically similar to that in Sec. II. The reason is that the warp factor is also a platform-type and the effective potential for gravitational perturbations is basically same as in Sec. II.

B. Echoes in Five-Dimensional Non-minimally Derivative Coupling Scalar-Tensor Theory

In this section, we investigate the echoes of the thick brane in a five-dimensional non-minimally derivative coupling scalar-tensor theory. First, the action of the five-dimensional



(a) The echoes in the $f(R)$ braneworld



(b) The echoes in the GR braneworld

Figure 16: Plots of the evolution $H(t, z)$ of a Gaussian wave packet. The parameters of the Gaussian wave packet are $\sigma = 0.5$ and $z_0 = -40$.

non-minimally derivative coupling scalar-tensor theory is given by [77, 78]

$$S = \int d^5x \sqrt{-g} \left[\frac{1}{2} F(\phi) R - b G_{MN} \nabla^M \phi \nabla^N \phi - \frac{1}{2} \partial^M \phi \partial_M \phi - V(\phi) \right]. \quad (43)$$

Varying the action (43) with respect to the metric g_{MN} , we obtain the gravitational field equation:

$$F(\phi) G_{MN} - \nabla_M \nabla_N F(\phi) + g_{MN} \square^{(5)} F(\phi) = T_{MN} + 2b \Theta_{MN}, \quad (44)$$

$$T_{MN} = \nabla_M \phi \nabla_N \phi - \frac{1}{2} g_{MN} (\nabla \phi)^2 - g_{MN} V(\phi), \quad (45)$$

$$\begin{aligned} \Theta_{MN} = & -\frac{1}{2} \nabla_M \phi \nabla_N \phi R + 2 \nabla_K \phi \nabla_{(M} \phi R_{N)}^K - \frac{1}{2} (\nabla \phi)^2 G_{MN} \\ & + \nabla^K \phi \nabla^L \phi R_{MKNL} + \nabla_M \nabla^K \phi \nabla_N \nabla_K \phi - \nabla_M \nabla_N \phi \square^{(5)} \phi \\ & + g_{MN} \left[-\frac{1}{2} \nabla^K \nabla^L \phi \nabla_K \nabla_L \phi + \frac{1}{2} (\square^{(5)} \phi)^2 - \nabla_K \phi \nabla_L \phi R^{KL} \right], \end{aligned} \quad (46)$$

where $\square^{(5)} = g_{MN} \nabla^M \nabla^N$. Unlike Eq. (6) in Sec. II, for Eq. (44), we find that the warp factor $e^{A(y)}$ can have a multi-peak shape solution. We can have a set of solutions given by

$$A(y) = \ln \left(\frac{\cosh d}{2} (\operatorname{sech}(ky + d) + \operatorname{sech}(ky - d)) \right), \quad (47)$$

$$\phi(y) = \tanh(ky). \quad (48)$$

Figure 17 shows that the influence of the distance d between the two peaks of the warp

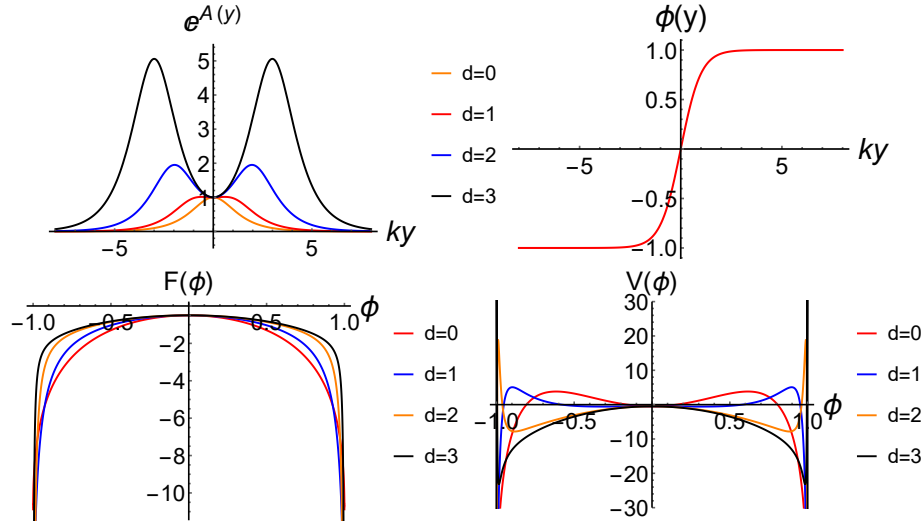


Figure 17: Plots of the warp factor e^A , the scalar field ϕ , the function $F(\phi)$ of the scalar field, and the scalar potential $V(\phi)$ with different peak distance d of the warp factor for the theory(43).

factor on the function $F(\phi)$ and the scalar potential $V(\phi)$. As d increases, the shape of $F(\phi)$ becomes flatter near $\phi = 0$ and the sides become steeper, and the two peaks of the scalar potential $V(\phi)$ become higher and closer to $\phi = 1$. Under the conformal coordinate z , the equation of the gravitational tensor perturbation is

$$K(z)\partial_z^2 h_{\mu\nu} + L(z)\partial_z h_{\mu\nu} + \square^{(4)} h_{\mu\nu} = 0, \quad (49)$$

where

$$K(z) = \frac{F - be^{-2A}(\partial_z \phi)^2}{F + be^{-2A}(\partial_z \phi)^2}, \quad (50)$$

$$L(z) = \frac{3\partial_z A(F - be^{-2A}(\partial_z \phi)^2) + \partial_z(F - be^{-2A}(\partial_z \phi)^2)}{F + be^{-2A}(\partial_z \phi)^2}. \quad (51)$$

Then making another coordinate transformations $dz = \sqrt{K(z)}dw$ and using the following decomposition:

$$h_{\mu\nu}(x^i, t, w) = \varepsilon_{\mu\nu}(x^i)T(w, t), \quad (52)$$

we can simplify the perturbation equation as

$$\partial_t^2 T - \partial_w^2 T + Q(w)\partial_w T + m^2 T = 0. \quad (53)$$

where $Q(w) = \frac{L}{\sqrt{K}} - \frac{\partial_w K}{2K}$. Redefining $T(t, w) = \exp(-\frac{1}{2} \int Q(w)dw)H(t, w)$, we further have

$$\partial_t^2 H - \partial_w^2 H + V_{\text{eff}}(w)H = -p^2 H, \quad (54)$$

where

$$V_{\text{eff}}(w) = \frac{1}{2}\partial_w Q + \frac{1}{4}Q^2. \quad (55)$$

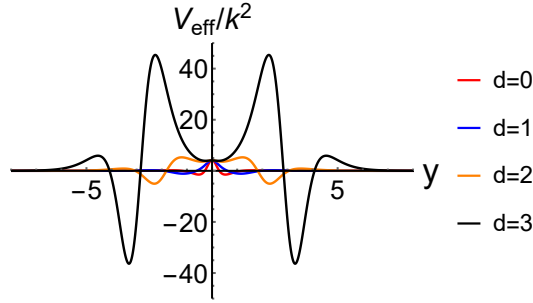
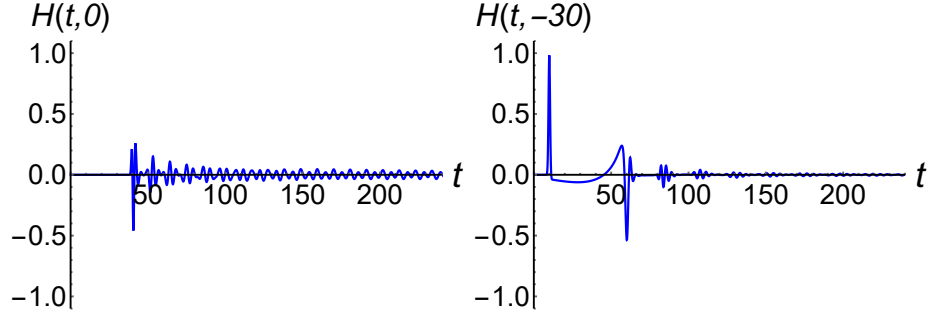


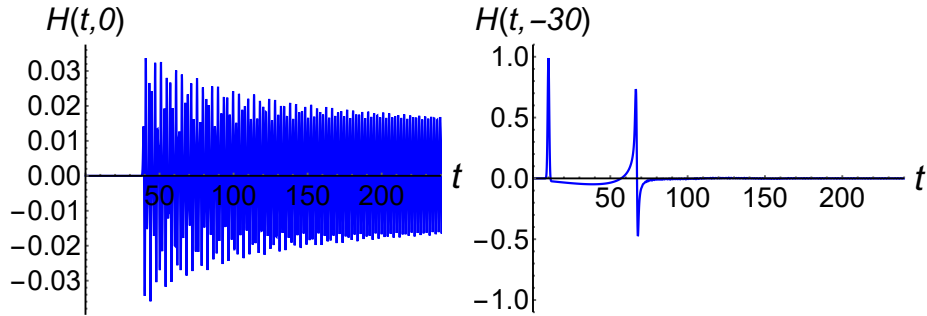
Figure 18: Plots of the effective potential (55) of the gravitational perturbation in five dimensional non-minimally derivative coupling theory.

In Fig. 18, it can be seen that the distance between the effective potential barriers, and the height of the effective potential barriers increase with d . Taking the same radiative boundary conditions as in Sec. II, we evaluate a Gaussian wave packet $H(0, w) = e^{-\frac{(w-w_0)^2}{\sigma}}$.

The results of the evolution are shown in Fig. 19(b). After the initial pulse, there are still several pulses, and the first echo is obvious but the amplitude of the later echoes are too small. The gravitational echoes observed at the outer regions of the brane are also more obvious than those inside the brane. Due to the small distance between the two barriers, the waveform reflects back and forth in a short time, leading to a relatively compact waveforms at points on the brane. The wave evolution on the brane gradually stabilizes, and exhibits a relatively slow decay. However, the height of the barrier varies greatly with distance d , which can be seen from Fig. 18. This variation results in higher reflectivity of the barrier for larger values of d , thereby making the first echo more pronounced. If it is a gravitational wave propagating on the brane, the energy outflow rate is extremely low, and the echoes are more obvious.



(a) The echoes in the GR braneworld



(b) The echoes in the five-dimensional non-minimally derivative coupling

theory

Figure 19: Plots of the evolution $H(t, w)$ of a Gaussian wave packet at fixed point. The parameters of the Gaussian wave packet and the effective potential are set to $\sigma = 0.5$, $w_0 = -40$, and $d = 3$.

IV. CONCLUSION

In this paper, we investigated the gravitational echoes in various extra-dimensional theories. In thick brane models, the effective potential of gravitational perturbations typically displays a multi-barrier form. Consequently, the propagation of the gravitational waves in most thick brane models may lead to the gravitational echoes. We studied the gravitational echoes in three different thick brane models. Additionally, we examined the impact of various parameters on the echoes in these models. Based on these investigations, we explored the propagation of the gravitational echoes on the brane, which allows us to make some constraints on the parameters of the extra-dimensional theories.

We investigated the thick brane generated by a background scalar field within the framework of general relativity. When the background scalar field is a double kink configuration, the warp factor of the metric exhibits a platform shape, thus enabling gravitational perturbations to possess an effective potential characterized by a distinct double barrier. The

distance b between two kinks of the scalar field and the vacuum expectation value v affect both the height and width of the effective potential barriers. We used Gaussian wave packets as initial data to study the time evolution of the gravitational waves in Eq. (15). It becomes evident that the distance between barriers influences the time interval between the two pulses of the echoes. Furthermore, the height of the barriers affects the reflectivity of the waves and the amplitude of the echo pulse. Different frequency components of Gaussian wave packets exhibit different reflectivities, which will affect the amplitude of the echoes.

Additionally, we explored the propagation of a Gaussian wave packet on the brane. The two-dimensional evolution equation is given by Eq. (27). If the gravitational waves are originated from a wave source on the brane, multiple gravitational wave signals can be detected at different locations on the brane due to reflections by barriers. The strength of these signals depends on the reflectivity. We also compute the time interval between the n -th echo signal and the primary wave.

We also conducted a brief calculation of the gravitational echoes in other two thick brane models. For the $f(R)$ thick brane, there is also the gravitational echo phenomenon. However, for the non-minimally derivative coupled scalar-tensor theory, the reflectivity of waves markedly increases due to the significant impact of the parameter d on the barriers. Therefore the gravitational waves inside the brane are notably challenging to escape, while those external to the brane become highly detectable upon their initial reflection.

Based on the existence of the gravitational echoes in the evolution of Gaussian wave packets in the three models, it can be deduced that gravitational echoes may be a common phenomenon in most thick brane models. The gravitational echoes in the thick brane occurs during propagation, and the frequency and amplitude of the echoes only depend on the initial wave and the structure of the thick brane models. In contrast, echoes from black holes or other compact stars are generated near the stars, with their frequency and amplitude being influenced by the initial wave and the spacetime structure of the stars themselves. Consequently, the attenuation rate of the same frequency in gravitational echoes remains consistent for different events' gravitational wave signals in the thick brane model. We expect to observe gravitational echoes in future gravitational wave detectors and to detect same behavior in different gravitational echo signals. This would help us understand more deeply on higher-dimensional spacetime theories. Next, we aim to investigate the gravitational echoes of non-flat brane and brane black hole models.

Acknowledgments

We are thankful to Bin Guo, Yu-Peng Zhang, and Qan Tan for useful discussions. This work was supported by the National Key Research and Development Program of China (Grant No. 2020YFC2201503), the National Natural Science Foundation of China (Grants No. 11875151, No. 12247101, and No.12205129), the 111 Project under (Grant No. B20063), the China Postdoctoral Science Foundation (Grant No. 2021M701529), the Major Science and Technology Projects of Gansu Province, and Lanzhou City's scientific research funding subsidy to Lanzhou University..

-
- [1] B. P. Abbott et al. (LIGO Scientific, Virgo), *Phys. Rev. Lett.* **116**, 061102 (2016), 1602.03837.
 - [2] B. P. Abbott et al. (LIGO Scientific, Virgo), *Phys. Rev. Lett.* **119**, 161101 (2017), 1710.05832.
 - [3] R. Abbott et al. (LIGO Scientific, Virgo), *Phys. Rev. Lett.* **125**, 101102 (2020), 2009.01075.
 - [4] L.-F. Wang, S.-J. Jin, J.-F. Zhang, and X. Zhang, *Sci. China Phys. Mech. Astron.* **65**, 210411 (2022), 2101.11882.
 - [5] Z.-K. Guo, *Sci. China Phys. Mech. Astron.* **65**, 210431 (2022).
 - [6] X. Wang, Y.-l. Zhang, R. Kimura, and M. Yamaguchi, *Sci. China Phys. Mech. Astron.* **66**, 260462 (2023), 2209.12911.
 - [7] Z. Yi, Q. Gao, Y. Gong, Y. Wang, and F. Zhang, *Sci. China Phys. Mech. Astron.* **66**, 120404 (2023), 2307.02467.
 - [8] R.-G. Cai, *Sci. China Phys. Mech. Astron.* **66**, 260461 (2023).
 - [9] S. Lin, B. Hu, X.-H. Zhang, and Y.-X. Liu, *Sci. China Phys. Mech. Astron.* **66**, 299512 (2023), 2212.14519.
 - [10] C. V. Vishveshwara, *Nature* **227**, 936 (1970).
 - [11] S. Chandrasekhar, *Fundam. Theor. Phys.* **9**, 5 (1984).
 - [12] K. D. Kokkotas and B. G. Schmidt, *Living Rev. Rel.* **2**, 2 (1999), gr-qc/9909058.
 - [13] T. Regge and J. A. Wheeler, *Phys. Rev.* **108**, 1063 (1957).
 - [14] V. Cardoso, E. Franzin, and P. Pani, *Phys. Rev. Lett.* **116**, 171101 (2016), 1602.07309.
 - [15] E. W. Leaver, *Phys. Rev. D* **41**, 2986 (1990).
 - [16] J. W. Guinn, C. M. Will, Y. Kojima, and B. F. Schutz, *Class. Quant. Grav.* **7**, L47 (1990).

- [17] E. Berti and K. D. Kokkotas, *Phys. Rev. D* **68**, 044027 (2003), hep-th/0303029.
- [18] X. Zhang, M. Wang, and J. Jing, *Sci. China Phys. Mech. Astron.* **66**, 100411 (2023), 2307.10856.
- [19] O. Lunin and S. D. Mathur, *Nucl. Phys. B* **623**, 342 (2002), hep-th/0109154.
- [20] K. Skenderis and M. Taylor, *Phys. Rept.* **467**, 117 (2008), 0804.0552.
- [21] A. Almheiri, D. Marolf, J. Polchinski, and J. Sully, *JHEP* **02**, 062 (2013), 1207.3123.
- [22] M. Saravani, N. Afshordi, and R. B. Mann, *Int. J. Mod. Phys. D* **23**, 1443007 (2015), 1212.4176.
- [23] P. Bueno, P. A. Cano, F. Goelen, T. Hertog, and B. Vercoocke, *Phys. Rev. D* **97**, 024040 (2018), 1711.00391.
- [24] V. Cardoso and P. Pani, *Nature Astron.* **1**, 586 (2017), 1709.01525.
- [25] V. Cardoso, S. Hopper, C. F. B. Macedo, C. Palenzuela, and P. Pani, *Phys. Rev. D* **94**, 084031 (2016), 1608.08637.
- [26] V. Cardoso and P. Pani, *Living Rev. Rel.* **22**, 4 (2019), 1904.05363.
- [27] R. S. Conklin, B. Holdom, and J. Ren, *Phys. Rev. D* **98**, 044021 (2018), 1712.06517.
- [28] J. Abedi, H. Dykaar, and N. Afshordi, *Phys. Rev. D* **96**, 082004 (2017), 1612.00266.
- [29] C. D. Capano, J. Abedi, S. Kastha, A. H. Nitz, J. Westerweck, Y.-F. Wang, M. Cabero, A. B. Nielsen, and B. Krishnan (2022), 2209.00640.
- [30] J. Abedi and N. Afshordi, *JCAP* **11**, 010 (2019), 1803.10454.
- [31] X. Zhong, W. Han, Z. Luo, and Y. Wu, *Sci. China Phys. Mech. Astron.* **66**, 230411 (2023), 2305.04478.
- [32] T. Kaluza, *Sitzungsber. Preuss. Akad. Wiss. Berlin (Math. Phys.)* **27**, 966 (1921).
- [33] O. Klein, *Z. Phys.* **37**, 895 (1926).
- [34] N. Arkani-Hamed, S. Dimopoulos, and G. R. Dvali, *Phys. Lett. B* **429**, 263 (1998), hep-ph/9803315.
- [35] L. Randall and R. Sundrum, *Phys. Rev. Lett.* **83**, 3370 (1999), hep-ph/9905221.
- [36] L. Randall and R. Sundrum, *Phys. Rev. Lett.* **83**, 4690 (1999), hep-th/9906064.
- [37] M. Gremm, *Phys. Lett. B* **478**, 434 (2000), hep-th/9912060.
- [38] W. D. Goldberger and M. B. Wise, *Phys. Rev. Lett.* **83**, 4922 (1999), hep-ph/9907447.
- [39] O. DeWolfe, D. Z. Freedman, S. S. Gubser, and A. Karch, *Phys. Rev. D* **62**, 046008 (2000), hep-th/9909134.

- [40] D. Bazeia, A. R. Gomes, L. Losano, and R. Menezes, *Phys. Lett. B* **671**, 402 (2009), 0808.1815.
- [41] C. Charmousis, R. Emparan, and R. Gregory, *JHEP* **05**, 026 (2001), hep-th/0101198.
- [42] O. Arias, R. Cardenas, and I. Quiros, *Nucl. Phys. B* **643**, 187 (2002), hep-th/0202130.
- [43] C. Barcelo, C. Germani, and C. F. Sopuerta, *Phys. Rev. D* **68**, 104007 (2003), gr-qc/0306072.
- [44] D. Bazeia and A. R. Gomes, *JHEP* **05**, 012 (2004), hep-th/0403141.
- [45] O. Castillo-Felisola, A. Melfo, N. Pantoja, and A. Ramirez, *Phys. Rev. D* **70**, 104029 (2004), hep-th/0404083.
- [46] S. Kanno and J. Soda, *JCAP* **07**, 002 (2004), hep-th/0404207.
- [47] N. Barbosa-Cendejas and A. Herrera-Aguilar, *JHEP* **10**, 101 (2005), hep-th/0511050.
- [48] P. Koerber, D. Lust, and D. Tsimpis, *JHEP* **07**, 017 (2008), 0804.0614.
- [49] N. Barbosa-Cendejas, A. Herrera-Aguilar, M. A. Reyes Santos, and C. Schubert, *Phys. Rev. D* **77**, 126013 (2008), 0709.3552.
- [50] M. C. Johnson and M. Larfors, *Phys. Rev. D* **78**, 083534 (2008), 0805.3705.
- [51] Y.-X. Liu, Y. Zhong, Z.-H. Zhao, and H.-T. Li, *JHEP* **06**, 135 (2011), 1104.3188.
- [52] A. E. R. Chumbes, J. M. Hoff da Silva, and M. B. Hott, *Phys. Rev. D* **85**, 085003 (2012), 1108.3821.
- [53] A. A. Andrianov, V. A. Andrianov, and O. O. Novikov, *Phys. Part. Nucl.* **44**, 190 (2013), 1210.3698.
- [54] M. Kulaxizi and R. Rahman, *JHEP* **10**, 193 (2014), 1409.1942.
- [55] A. de Souza Dutra, G. P. de Brito, and J. M. Hoff da Silva, *Phys. Rev. D* **91**, 086016 (2015), 1412.5543.
- [56] S. Chakraborty and S. SenGupta, *Eur. Phys. J. C* **76**, 648 (2016), 1511.00646.
- [57] A. Karam, A. Lykkas, and K. Tamvakis, *Phys. Rev. D* **97**, 124036 (2018), 1803.04960.
- [58] J. Westerweck, A. Nielsen, O. Fischer-Birnholtz, M. Cabero, C. Capano, T. Dent, B. Krishnan, G. Meadors, and A. H. Nitz, *Phys. Rev. D* **97**, 124037 (2018), 1712.09966.
- [59] R. K. L. Lo, T. G. F. Li, and A. J. Weinstein, *Phys. Rev. D* **99**, 084052 (2019), 1811.07431.
- [60] G. Ashton, O. Birnholtz, M. Cabero, C. Capano, T. Dent, B. Krishnan, G. D. Meadors, A. B. Nielsen, A. Nitz, and J. Westerweck (2016), 1612.05625.
- [61] A. B. Nielsen, C. D. Capano, O. Birnholtz, and J. Westerweck, *Phys. Rev. D* **99**, 104012 (2019), 1811.04904.
- [62] N. Uchikata, H. Nakano, T. Narikawa, N. Sago, H. Tagoshi, and T. Tanaka, *Phys. Rev. D*

- 100**, 062006 (2019), 1906.00838.
- [63] Y.-T. Wang and Y.-S. Piao (2020), 2010.07663.
- [64] E. Halyo (1999), hep-th/9909127.
- [65] A. Chamblin and G. W. Gibbons, *Phys. Rev. Lett.* **84**, 1090 (2000), hep-th/9909130.
- [66] Y.-X. Liu, L.-D. Zhang, S.-W. Wei, and Y.-S. Duan, *JHEP* **08**, 041 (2008), 0803.0098.
- [67] V. A. Rubakov and M. E. Shaposhnikov, *Phys. Lett. B* **125**, 136 (1983).
- [68] M. Megevand, I. Olabarrieta, and L. Lehner, *Class. Quant. Grav.* **24**, 3235 (2007), 0705.0644.
- [69] R. A. Isaacson, *Phys. Rev.* **166**, 1263 (1968).
- [70] R. A. Isaacson, *Phys. Rev.* **166**, 1272 (1968).
- [71] V. Pavlidou, K. Tassis, T. W. Baumgarte, and S. L. Shapiro, *Phys. Rev. D* **62**, 084020 (2000), gr-qc/0007019.
- [72] M. Alcubierre, B. Bruegmann, P. Diener, M. Koppitz, D. Pollney, E. Seidel, and R. Takahashi, *Phys. Rev. D* **67**, 084023 (2003), gr-qc/0206072.
- [73] M. Parry, S. Pichler, and D. Deeg, *JCAP* **04**, 014 (2005), hep-ph/0502048.
- [74] Y. Zhong, Y.-X. Liu, and K. Yang, *Phys. Lett. B* **699**, 398 (2011), 1010.3478.
- [75] H. Yu, Y. Zhong, B.-M. Gu, and Y.-X. Liu, *Eur. Phys. J. C* **76**, 195 (2016), 1506.06458.
- [76] A. de Souza Dutra, A. C. A. de Faria, Jr., and M. Hott, *Phys. Rev. D* **78**, 043526 (2008), 0807.0586.
- [77] Q.-M. Fu, H. Yu, L. Zhao, and Y.-X. Liu, *Phys. Rev. D* **100**, 124057 (2019), 1907.12049.
- [78] F. A. Brito and F. F. Santos, *Eur. Phys. J. Plus* **137**, 1051 (2022), 1810.08196.